Int. J. on Recent Trends in Engineering and Technology, Vol. 6, No. 2, Nov 2011

Wind speed measurement from Shack Hartmann Wavefront Sensor data: An experimental review of cross-correlation peak detection

M. B. Roopashree, Akondi Vyas, B. Raghavendra Prasad
Indian Institute of Astrophysics, II Block, Koramangala, Bangalore 560 034, India

***Abstract*—The mean velocity of the atmospheric wind is an important parameter in characterizing the turbulence above an astronomical telescope. Real-time wind velocity measurement is exceedingly essential to update the design metrics of the adaptive optics system periodically to improve the dynamic performance. A Shack Hartmann Wavefront Sensor (SHWS), which is generally used in astronomical telescope adaptive optics systems for wavefront sensing, can be simultaneously used for wind speed estimation and this means of wind speed estimation needs special attention due to the ease of its implementation. In this paper, we discuss in elaborate the experimental evaluation of the wind measurement from the calculation of the two dimensional cross-correlation function. Adopting the peak technique, we find that the identification of the peak can be made accurate by using the computation cost effective 3-point parabolic interpolation technique, which is shown to behave close to the 3-point Gaussian interpolation. Also, it is shown that the time interval chosen for the calculation of the cross-correlation plays a vital role in optimal performance. For small time interval case, the interpolation techniques do not yield correct results. In this case, it is shown that the iteratively weighted center of gravity algorithm is more suitable.**

***Index Terms*—adaptive optics, Shack Hartmann wavefront sensor, atmospheric turbulence, wind speed, astronomical telescopes**

I. Introduction

Astronomical observations using terrestrial large telescopes are hindered by the optical refractive index variations caused by atmospheric turbulence [1]. Atmospheric wind speed that primarily contributes to the mixing of warm and cold air in the atmosphere plays a vital role in deciding the atmospheric seeing at a given observatory [2]. Technological advancements in the field of astronomical adaptive optics over the last few decades paved the way to high resolution astronomical imaging [3]. The temporal fluctuations in the transverse wind velocity and variations in the measured Fried parameter severely affect the optimal design metrics and hence the performance of adaptive optical systems [4,5]. The servo lag errors are minimized by using prediction algorithms [6-9]. The temporal fluctuations affect the control metrics in these algorithms too [10]. Thus, a real-time measurement of the optical refractive index statistics and transverse wind velocity is inevitable to facilitate the monitoring of the atmospheric turbulence. The information provided by the real-time measurements can be used to employ dynamic changes in the optical design for the best operation of astronomical adaptive optics systems.

Early methods used the drift of scintillation pattern resulting from the traversing refractive index irregularities for the measurement of transverse wind speed [11]. In the case of optical measurements, wind velocity is determined from the covariance function of scintillations of a plane wave [12]. Several other methods were gradually developed for the remote measurement of wind across the line of sight [13-16]. A method of path-averaged crosswind calculation via the measurement of the time lagged covariance function using detectors placed at a known separation is described by Ting-i Wang, et. al [17]. Also, they compare different methods in terms of their ease of implementation and immunity to observational errors and non-uniformity of the atmosphere. These scintillation techniques are capable of measuring very small velocities. A slight modification of this technique based on crossed laser beams can be used to estimate the wind velocity profiles [15]. Most of these methods have been numerically tested based on the simulation of atmosphere-like phase screens [18].

Similar to the use of cross correlation properties of the intensity of optical fields in determining wind velocity, one can also make use of the cross-correlation of wavefront phase [19]. Two spatially separated point sources and two wavefront sensors can be configured to obtain crossed optical paths which can be used for the calculation of wavefront phase correlation. Wind velocity profiles can be obtained by varying the separation between sensors and/or between point source. In the cases where the turbulent medium can be modeled as single or multi-layered, the real-time wavefront sensor measurements from a single guide star can be directly used for the determination of transverse wind speed [20]. The Shack Hartmann Wavefront Sensor (SHWS) has been regularly used for turbulence characterization [21,22].

In this paper, we experimentally validate the cross-correlation method based on peak identification to estimate the transverse wind speed using a SHWS. The cross-correlation peak occupies only a few discrete pixels and hence to identify the location of the peak, interpolation techniques are adopted.

The following section describes the optical arrangement employed to obtain the SHWS data experimentally. In section III, we present the results of the calibration of the phase plate that was used to simulate turbulence in the laboratory. Section IV describes the wavefront reconstruction procedure in the

DOI: 01.IJRTET.06.02.195

SHWS. In section V, various methods used for wind speed estimation from the calculated cross-correlation function are presented. In section VI, different peak identification techniques are described. Results of the analysis performed on the experimentally obtained data and conclusions are presented in sections VII and VIII.

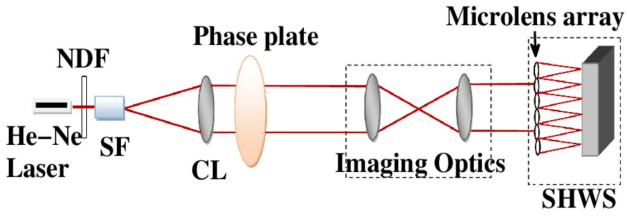

Figure 1. Experimental setup to obtain wavefront sensor data

II. Wavefront Sensor Data

The experimental setup used to obtain the wavefront sensor data is shown in Fig. 1. A 15mW Melles Griot He-Ne laser with a wavelength of λ = 632.8nm was used as the source of light. The laser beam was spatially filtered using a 40x objective lens and 5μm pinhole. It is then collimated using a doublet lens (CL) of focal length f = 15cm. The collimated beam was allowed to be incident on a phase plate. After passing through the phase plate, the distorted beam was sensed using a SHWS. The SHWS was made up of a microlens array and a CCD camera placed at the focal plane of the lenslet array. A neutral density filter (NDF) was placed in front of the laser source so as to control the intensity of light falling on the CCD camera. The microlens array is from Flexible Optical BV (OKO technologies) and is of size 2 × 2 cm^2 consisting of an array of 100 × 100 microlenses with 200μm pitch. The focal length of the microlenses is 4cm. A monochrome progressive scan CCD camera (Pulnix TM 1325-CL) placed at the focal plane captures the spot pattern. Initial characterization results have been presented earlier [23].

The phase plate that was used in our experiment is a pseudo random phase screen designed by Lexitek, with the optical path difference defined over an annular region of a 4096 × 4096 array. The phase map was made with a Near-Index-Match™ optic. The Fried parameter of the phase plate is 400μm at a wavelength of 633nm. The phase map design of the phase plate assumes the Kolmogorov model of atmospheric turbulence. Since the active detector area is 8.4 × 6.7 mm^2, it is also the useful optical beam size. Hence, only a small portion of the phase screen is seen by the SHWS at a given instant. This corresponds to a smaller portion of the microlens array (~ 42 × 33 lenses). The dynamic behavior of atmospheric turbulence was realized in the laboratory by fixing the phase plate on a rotary stage and driving it with the help of a calibrated motor. The rotation speed of the phase screen is varied to achieve different velocities. The experimental conditions correspond to a single layer atmospheric turbulence model with a fixed wind speed, where Taylor frozen flow hypothesis is completely valid. The background noise caused because of stray light can be effectively eliminated by capturing a background image in the absence of microlens array and phase plate (see Fig. 1). A reference focal spot pattern was taken by placing the microlens array in the absence of phase plate in the beam path. The background image is subtracted from the reference image and the spot pattern image taken with the phase plate in the beam path. The resultant images are then used for reconstructing the phase of the incident wavefronts.

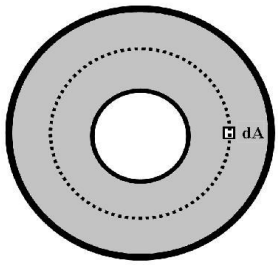

Figure 2. Small area approximation: Distance traveled in one rotation is equal to the perimeter of the dotted circle

III. Phase Plate Calibration

A. Phase plate to SHWS compatibility

It is important to design the wavefront sensing experiment in such a way that the SHWS and the wavefront sensing algorithm can efficiently detect the distortions introduced by the phase plate. The coherence length of the phase plate defined by the Fried parameter, r_0 in our case is 400μm. As the number of microlenses used for wavefront sensing is increased for a given area, the spatial sampling and spatial resolution are increased. Also, since the pitch of the microlens array used for wavefront sensing is 200μm, the sampling is being done at double the spatial frequency of phase plate distortions, given the unit magnification employed in the imaging optics (see Fig. 1).

B. Phase plate speed calibration

The phase plate is mounted on a rotary stage assembly, the movement is steered by a motor that is regulated using a Lexitek stepper controller. The controller, capable of standalone operation was directly used for changing the rotation speed. The command MVS sets the move speed and is quantized to multiples of 12.5 pulses per second (pps). A simple calibration procedure was carried out to measure the speed of the phase plate and test its linearity with changing move speed (MVS). The time taken for a single rotation of the phase plate was measured for different rotation speeds starting from 12.5 pps to 400 pps (see Table 1). Since the region of interest (ROI) occupies a very small area, dA (see Fig. 2), for the calculation of the speed, we made the approximation that the distance moved by the ROI in a single rotation is equal to the perimeter of the dotted circle in Fig. 2, which has a radius, r that is equal to the length of the line joining the center of the phase plate and the center of the ROI. In our phase plate, r=30mm and hence a one rotation distance of 188.4mm. Measurement of the time taken for a single rotation gives the speed of movement of the phase screen across the SHWS. The calibration plot of the speed of the rotary stage motor for different MVS is shown in Fig. 3.

DOI: 01.IJRTET.06.02.195

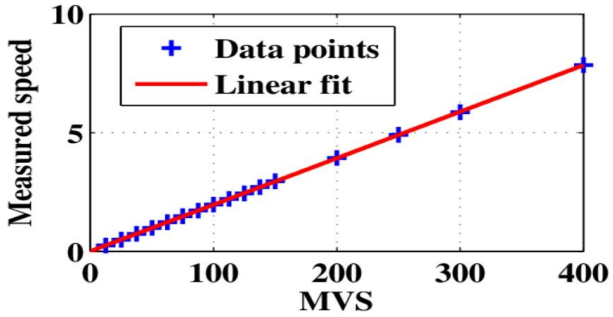

Figure 3. Calibration of the rotary stage speed with the MVS function in the motor controller

TABLE I. SPEED CALIBRATION OF THE ROTARY STAGE MOTOR

MVS	Time for one rotation (s)	Speed (in mm/s)
12.5	767.98	0.245
25.0	384.44	0.490
37.0	255.97	0.736
50.0	191.51	0.984
62.5	153.61	1.226
75.0	127.83	1.474
87.5	109.78	1.716
100.0	95.88	1.965
112.5	85.47	2.204
125.0	77.30	2.437
137.5	69.63	2.706
150.0	63.91	2.948
200.0	47.88	3.935
250.0	38.37	4.910
300.0	32.15	5.860
400.0	24.01	7.847

C. Scaling to astronomical dimensions

In order to check the suitability and applicability of the turbulence simulated using the phase plate and performing a numerical evaluation of the wind speed measurement techniques, it would be appropriate to scale the simulated turbulence to astronomical dimensions.

Comparing the case of a telescope situated at a site where r_0=25cm with the phase plate r_0=400μm, the beam downscaling in our experiment can be calculated to be 625:1. Thus, with the ROI being of dimensions ~5 × 5 mm^2 (25 × 25 microlenses used for sensing), the corresponding telescope aperture size would be of diameter 3.125m. From Table 1, it can be noted that with MVS = 400, the effective translation velocity of the phase plate across the detector is 7.847 mm/s. In realistic case, this would correspond to 4.9 m/s. Employing a faster CCD, it would be possible to analyze greater wind speeds (i.e., phase plate can be moved with greater MVS).

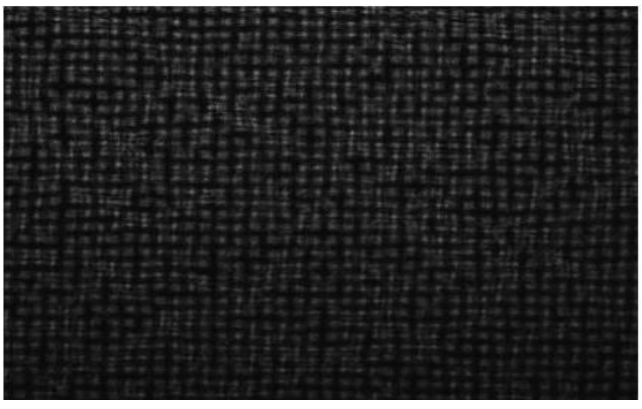

Figure 4. A sample spot pattern image captured by the SHWS camera with the phase plate in the beam path

IV. WAVEFRONT RECONSTRUCTION

The SHWS spot pattern images were captured at a rate of 30 frames per second. A single frame captured by the CCD camera is shown in Fig. 4. Using sequential data acquisition, a sequence of 100 images, with well defined time separation, were captured for a given rotation speed, and were arranged in the form of a data cube.

In order to choose a correct region of interest (ROI), we adopted a simple peak search algorithm from the image center to locate the central SHWS spot. The ROI was then selected appropriately so that a 25×25 SHWS spot pattern image is obtained. Once the background noise on the images is removed, centroiding is performed on individual spots to locate the centroids. At good light conditions (see Fig. 4), the simple center of gravity algorithm performs a decent job and we prefer to use this algorithm for centroiding [24]. The details of this algorithm are discussed in section VI C, with regard to the peak detection of the cross-correlation peak.

The difference in the centroid locations of the spot pattern and reference spot pattern gives the local slopes of the wavefront distortions across each microlens of the lenslet array. These local slopes from the wavefront sensor are used to reconstruct the wavefront shape. We used the iterative least square method for wavefront reconstruction [25]. A few samples of the phase maps that were obtained after applying the wavefront reconstruction algorithms are shown in Fig. 5.

The obtained wavefront phase maps are 25 × 25 sized matrices, each point on the array containing the relative phase value. Bilinear interpolation was used to re-size these phase maps to 100 × 100 sized matrices and are saved in the form of a data cube. The slope data and reconstructed wavefront phase data obtained in this manner was analyzed using different wind velocity measurement techniques to calculate the speed and compared with the known speed. The various methods employed in our work and the results of the wind velocity measurement are discussed in the following sections.

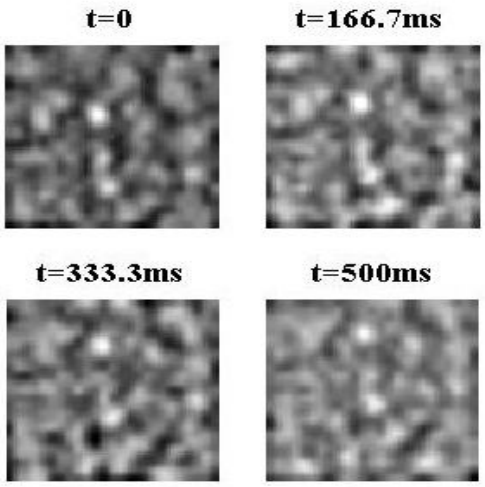

Figure 5. Grayscale maps of the reconstructed phase with MVS = 100

DOI: 01.IJRTET.06.02.195

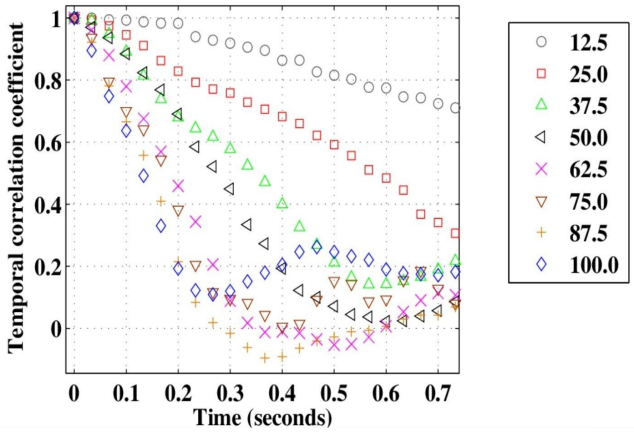

Figure 6. The decay of the correlation coefficient with time for different MVS

The correlation coefficient χ_k^1, can be used as a metric for comparison of time evolving reconstructed wavefronts. Here, '*k*' represents the time index and '1' in the superscript suggests that the comparison is always made with the first wavefront in the time sequence.

$$\chi_k^1 = \frac{E\left[\left(A^1 - \mu^1\right)\left(A_k - \mu_k\right)\right]}{\sigma^1 \sigma_k} \tag{1}$$

where, μ and σ correspond to mean and standard deviation respectively, and $1 \leq k \leq 100$. Fig. 6 shows a comparison of the temporal correlation coefficient for different MVS. The decay of the temporal correlation coefficient is slower in the case of MVS = 12.5 and very fast in the case of MVS = 100. Also, it should be noted that the decay rate of the temporal correlation coefficient increases with increasing move speed until the correlation coefficient drops below a value of 0.2, after which the behavior is random since the later wavefronts are completely different from the first wavefront (especially for MVS beyond 62.5 as shown in Fig. 6).

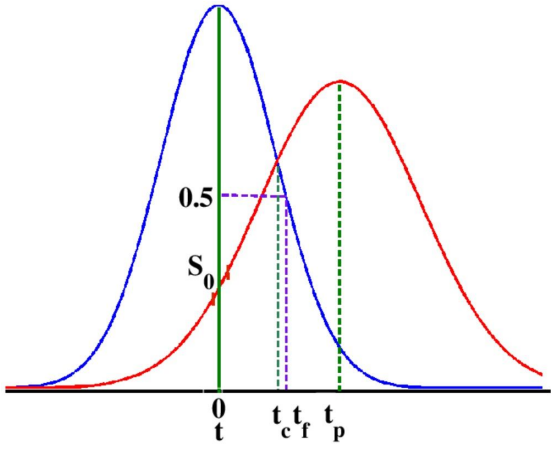

Figure 7. Auto-covariance (blue colored curve) and cross-covariance (red colored curve) functions

V. Wind speed measurement techniques from SHWS data

Fig. 7 shows the normalized time-lagged auto-covariance and cross-covariance functions as described by Ting-i Wang, et. al [17]. The horizontal axis stands for the time co-ordinate. The different parameters appeared in the plot and different wind velocity measurement techniques are described below,

t_p - time delay at the peak of the cross covariance curve;

t_c - cross over time delay of the auto covariance and cross covariance curves;

t_f - width of the auto covariance curve at half power point; and

S_0 - slope of the cross co-variance curve at zero time delay

Peak technique :

$$V_p \sim \frac{\rho}{t_p} \tag{2}$$

where ρ is the 'spatial separation at which the cross covariance is calculated.

Slope technique :

$$V_s \sim S_0 \tag{3}$$

Frequency technique :

$$V_f \sim \frac{1}{t_f} \tag{4}$$

Briggs technique :

$$V_b \sim \frac{\rho}{2t_c} \tag{5}$$

In this paper, we take a closer look at the peak identification technique and compare different algorithms in this respect. The cross-correlation matrix of two phase maps, P_1 and P_2 (of dimension 100×100 each separated by a time interval, ΔT), is obtained by spatially shifting (in discrete steps) one of the phase maps (say, P_1) to all possible locations and calculating its correlation coefficient with the non-shifted phase map (P_2) as described in equation (1).

VI. Peak detection techniques

Since the number of active pixels that are near the peak of the autocorrelation function, that contribute significantly to the accurate peak detection is generally small, a peak detection technique is required to accurately measure sub-pixel shifts of the cross-correlation peak. The identification of the auto-correlation peak and the cross-correlation peak can be done either using different interpolation or centroiding techniques. In this paper, two interpolation techniques, namely Gaussian and Parabolic are used. Also, the performance of three centroiding algorithms - center of gravity (CoG), weighted

DOI: 01.IJRTET.06.02.195

center of gravity (WCoG) and iteratively weighted center of gravity (IWCoG) is tested and compared with the interpolation techniques.

A. 3-point Gaussian Interpolant

The pixel location of the peak in the two dimensional correlation map is initially identified. We take two points on either side of the peak value along one axis (say '*x*' axis) and perform a Gaussian interpolation of three adjacent sample points. We used the Gaussian interpolator of the form,

$$f_G(x) = A\exp\left(-\frac{(x-x_0)^2}{2\sigma^2}\right) \tag{6}$$

we can compute 'x_0' the location of the Gaussian peak, from the following expression:

$$x_0 = \frac{1}{2}\left[\frac{R'-L'}{2M'-R'-L'}\right] \tag{7}$$

and

$$\sigma^2 = \frac{1}{2M'-R'-L'} \tag{8}$$

$$\log_{10} A = M' + \frac{x_0^2}{2\sigma^2} \tag{9}$$

The primed quantities, *R'*, *M'*, *L'* are the logarithmic values of $f_G(1)$, $f_G(0)$ and $f_G(-1)$ respectively. It can be observed that the shape of the cross-correlation function does not maintain a Gaussian shape at all times as can be seen in Fig. 8. Hence, better peak detection techniques are necessary.

B. 3-point Parabolic Interpolator

To obtain a resultant fit of the form,

$$f_p(k) = a\,(k-p)^2 + b \tag{10}$$

The coordinate location of the peak (in '*x*' axis) is evaluated using the following expression,

$$p = \frac{R-L}{2(2M-R-L)} \tag{11}$$

where, $f_p(-1)$=L, $f_p(0)$=M and $f_p(1)$=R. and

$$a = \frac{L+R-2M}{2} \tag{12}$$

$$b = M - \frac{1}{8}\left[\frac{(L-R)^2}{L+R-2M}\right] \tag{13}$$

In the case of a three point interpolator, the performance of Gaussian and parabolic interpolators is very close, unless the cross-correlation function is spread over less than 3×3 pixels. When a larger number of pixels around the neighbourhood of the cross-correlation peak are used for interpolation, the choice of the interpolator will be critical. Another advantage of the parabolic interpolator is its ease of computation.

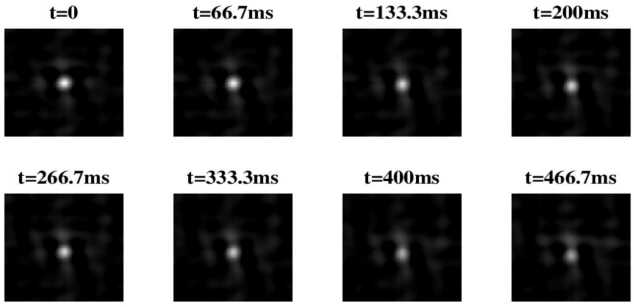

Figure 8. The change of shape in the two dimensional cross correlation function with time for the case of MVS=37. For the evaluation, the first wavefront was taken as reference for all the calculations here

C. Centroiding algorithms

For the cross-correlation matrix, $C(x,y)$, the location of the centroid (x_c,y_c) using the center of gravity (CoG) method is given by,

$$(x_c, y_c) = \frac{\sum_{ij} C_{ij} X_{ij}}{\sum_{ij} C_{ij}} \tag{14}$$

This simple peak detection technique works best with high signal to noise ratio on the cross-correlation matrix. The weighted center of gravity (WCoG) is a method that can take the advantage of the shape information of the cross-correlation function, is an improved version of the CoG technique.

$$(x_c, y_c) = \frac{\sum_{ij} W_{ij} C_{ij} X_{ij}}{\sum_{ij} W_{ij} C_{ij}} \tag{15}$$

The technique fails for very large shifts of the peak of the cross-correlation function and under poor signal levels. Here W_{ij} is the weighting function. The iterative technique (IWCoG) is a more accurate extension of the WCoG technique [26, 27]. This method is similar to the WCoG technique with a difference that the location of the center of the weighting function is iteratively revised in order to get closer to the actual location of the cross-correlation peak. After every iteration, the center of the weighting function is shifted to the location of the cross-correlation peak that is estimated by the previous iteration. This method of peak detection is best suited for noisy conditions and to resolve very close shifts in the peak of the cross-correlation function.

VII. Results

Once the location of the peak is identified, we are left with evaluating the wind velocity. It can be directly derived from the slope of the straight line that best fits the curve '*x* vs *t*' for individual MVS case as depicted in Fig. 9, for the case of parabolic interpolator. Here, the cross-correlation of wavefronts arriving at any time '*t*' is computed with respect to the wavefront that arrived at *t=0*. It can be observed from the graph that the *x*-position of the cross-correlation peak increases with time for a given MVS and beyond a certain

DOI: 01.IJRTET.06.02.195

time '*t*', the peak detection becomes difficult due to the reduced cross-correlation maximum. For this reason, we eliminate the inappropriate data beyond a certain time while fitting the '*x* vs *t*' curve with a straight line. The slope of the '*x* vs *t*' curve increases with increasing MVS. The maximum distance traveled along the '*x*' direction by the cross-correlation peak is nearly 2mm. The choice of the ROI at the location as indicated in Fig. 2 suggests that the shift in the peak will occur essentially due to the motion along a single direction. Similarly, the maximum shift along the '*y*' direction can be calculated to be nearly 350μm. This small shift along the '*y*' direction is due to the finite width of the ROI (Fig. 2). A comparison of different peak detection techniques is shown in Fig. 10. Clearly, the overlapping Gaussian interpolator and parabolic interpolator suggests their similarity for the 3-point interpolation applied here for both cases. The CoG and WCoG methods completely fail in estimating the wind speed. This is attributed to the presence of noise in the cross-correlation matrices (see Fig. 8).

The wind speed is estimated from the measured slope values of the curve '*x* vs *t*', and are tabulated in Table II for parabolic interpolator and IWCoG based cross-correlation peak detection methods. The wind velocity is calculated from the slope value of the '*x* vs *t*' curve by multiplying 0.05 to it, so as to account for the bilinear interpolation performed to re-size the phase maps from 25×25 array to 100×100 matrix.

A study of the optimum time interval selection for the best estimation of wind speed for different MVS is shown in Fig. 11. This graph suggests that at very small time intervals, the measured velocity is higher than the actual (see Table I) for all MVS, with MVS=12.5 most affected. Hence, for lower wind speeds, the selection of a larger interval is more appropriate. This is because at lower MVS (lower wind speed), the phase plate (wavefront) moves slower and hence decaying the correlation coefficient at a slower rate. The slow decay rate of the correlation coefficient (see Fig. 6) also indicates that the shift in the peak of the cross-correlation function is small within a small interval of time. If this shift is so small that the cross-correlation peaks cannot be resolved, the resultant measured wind speed can be erroneous. At very large time intervals and faster wind speeds, the selection of a lower time interval is better, for, we are at the risk of decorrelating the wavefronts completely if we choose a large time interval.

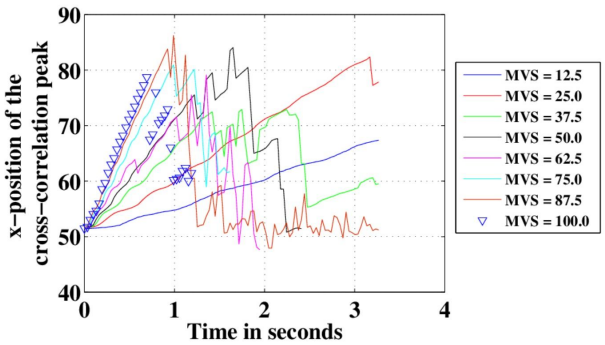

Figure 9. Parabolic interpolator: The movement of the x-coordinate of the cross correlation peak with time at different wind speed

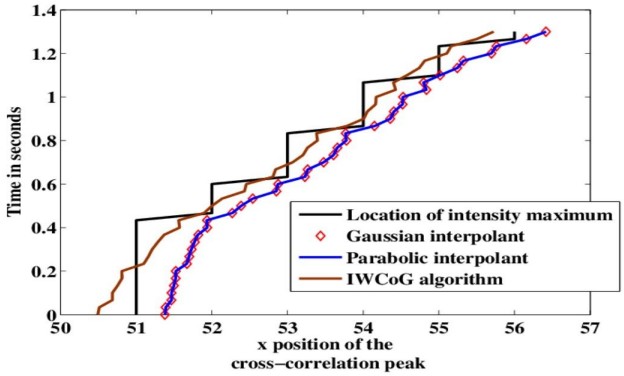

Figure 10. Comparison of peak detection techniques

At small time intervals, the IWCoG method performs better than the parabolic interpolation method. This can be concluded from the slope of the '*x* vs *t*' curve at low '*t*' for IWCoG in comparison with that for parabolic interpolation (see Fig.10). Hence, IWCoG is sensitive to very small shifts in the peak of the cross-correlation method. In this paper, we have taken the Gaussian function as the weighting function in the IWCoG. Since the shape of the surface near the cross-correlation peak does not resemble the Gaussian for wavefronts with large time interval difference, IWCoG with a Gaussian weighting function is not suitable in such a case. Also, with a faster CCD, it is possible to record wavefronts at a faster rate. To take advantage of this fast nature of the detector, we need algorithms that detect the very small shifts in the cross correlation peak. A more rigorous analysis of the IWCoG method is necessary on the choice of weighting function, optimization of the iterations to improve the performance of the IWCoG method.

As a test of repeatability, five different sets of data were analyzed for each MVS listed in Table II. It was observed that the measured wind speed was reasonably consistent with the standard deviation reducing as MVS is increased.

TABLE II. MEASURED WIND SPEED

MVS	Actual Speed (mm/s)	Parabolic (in mm/s)	IWCoG (in mm/s)
12.5	0.245	0.260	0.227
25.0	0.490	0.509	0.403
37.0	0.736	0.769	0.656
50.0	0.984	1.030	0.894
62.5	1.226	1.175	1.084
75.0	1.474	1.506	1.300
87.5	1.716	1.801	1.555
100.0	1.965	2.089	1.483

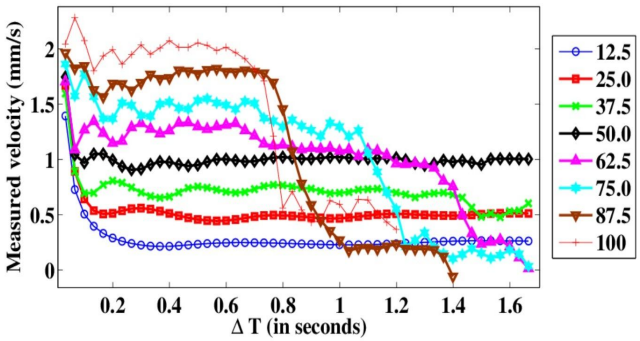

Figure 11. Parabolic interpolator: Study on the optimal choice of the time interval for wind velocity measurement at different MVS

DOI: 01.IJRTET.06.02.195

A plot of the measured wind speed against the actual value is shown in Fig. 12. In this plot, the data points lie along the diagonal, validating the implemented peak detection algorithms.

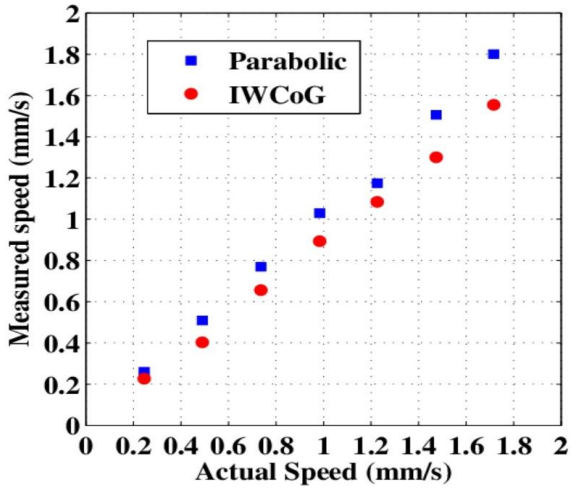

Figure 12. Validation of the parabolic interpolation and IWCoG based peak identification methods for wind velocity measurement in comparison with the actual velocity

VIII. Conclusion

In this paper, the cross correlation peak identification technique for wind speed estimation from SHWS data is implemented. Experimental data was obtained using the static phase plate which is mounted on a rotary stage and a laboratory SHWS. It is shown that the 3-point parabolic interpolation can be effectively used for the detection of the location of the cross-correlation peak. Optimization of the time interval that best suits with the implemented technique suggests that this method is not very sensitive to small shifts in the cross-correlation peak.

In the future, we would like to make a further detailed comparison of the peak detection technique with the other wind estimation methods, including - slope technique, frequency technique and Briggs technique which are mentioned in section V. Attempts will be made to improve the accuracy in peak detection of the cross-correlation function using better algorithms.

Acknowledgement

We thank Dr. Ravinder Kumar Banyal, Indian Institute of Astrophysics, for useful discussions and support.

References

[1] J. W. Hardy, *Adaptive optics for astronomical telescopes*. Oxford University Press, USA, 1998.

[2] B. Garca-Lorenzo, A. Eff-Darwich, J. J. Fuensalida, and J. Castro-Almazn, "Adaptive optics parameters connection to wind speed at the teide observatory: corrigendum," *Monthly Notices of the Royal Astronomical Society*, vol. 414, no. 2, pp. 801–809, 2011. [Online]. Available:http://dx.doi.org/10.1111/j.1365-2966.2011.17787.x

[3] M. Hart, "Recent advances in astronomical adaptive optics," *Appl. Opt.*, vol. 49, no. 16, pp. D17–D29, Jun 2010. [Online]. Available: http://ao.osa.org/abstract.cfm?URI=ao-49-16-D17

[4] L. Z. Kennedy and J. W. Bilbro, "Remote measurement of the transverse wind velocity component using a laser doppler velocimeter," *Appl. Opt.*, vol. 18, no. 17, pp. 3010–3013, Sep 1979. [Online]. Available:http://ao.osa.org/abstract.cfm?URI=ao-18-17-3010G.

[5] S. G. Els, T. Travouillon, M. Schck, R. Riddle, W. Skidmore, J. Seguel, E. Bustos, and D. Walker, "Thirty meter telescope site testing vi: Turbulence proûles," *Publications of the Astronomical Society of the Paciûc*, vol. 121, no. 879, pp. pp. 527–543, 2009. [Online].Available: http://www.jstor.org/stable/10.1086/599384

[6] L. C. Johnson, D. T. Gavel, and D. M. Wiberg, "Bulk wind estimation and prediction for adaptive optics control systems," *J. Opt. Soc. Am. A*, vol. 28, no. 8, pp. 1566–1577, Aug 2011. [Online]. Available:http://josaa.osa.org/abstract.cfm?URI=josaa-28-8-1566

[7] A. Vyas, M. B. Roopashree, and B. R. Prasad, "Progressive prediction of turbulence using wave front sensor data in adaptive optics using data mining," *International Journal of Power, Control Signal Computation*, 2011.

[8] A. Vyas, M. B. Roopashree, and B. R. Prasad, "Extrapolating zernike moments to predict future optical wavefronts in adaptive optics using real time data mining," *Journal of Communication and Computer*, vol. 8, no. 3, pp. 173–179, March 2011.

[9] L. A. Poyneer and J.-P. Veran, "Toward feasible and effective predictive wavefront control for adaptive optics," N. Hubin, C. E. Max, and P. L. Wizinowich, Eds., vol. 7015, no. 1. *SPIE*, 2008, p. 70151E. [Online]. Available:http://link.aip.org/link/?PSI/7015/70151E/1

[10] A. Vyas, M. B. Roopashree, and B. R. Prasad, "Efûcient minimization of servo lag error in adaptive optics using data stream mining," in *Advances in Power Electronics and Instrumentation Engineering*, ser. Communications in Computer and Information Science, V. V. Das, N. Thankachan, and N. C. Debnath, Eds. Springer Berlin Heidelberg, 2011, vol. 148, pp. 13–18.

[11] R. S. Lawrence, G. R. Ochs, and S. F. Clifford, "Use of scintillations to measure average wind across a light beam," *Appl. Opt.*, vol. 11, no. 2, pp. 239–243, Feb 1972. [Online]. Available: http://ao.osa.org/abstract.cfm?URI=ao-11-2-239

[12] A. Peskoff, "Theory for remote sensing of wind-velocity proûles," *Proceedings of the IEEE*, vol. 59, no. 2, pp. 324 – 326, Feb. 1971.

[13] V. A. Banakh and D. A. Marakasov, "Wind velocity proûle reconstruction from intensity ûuctuations of a plane wave propagating in a turbulent atmosphere," *Opt. Lett.*, vol. 32, no. 15, pp. 2236–2238, Aug 2007. [Online]. Available:http://ol.osa.org/abstract.cfm?URI=ol-32-15-2236

[14] S. C. Koefûer and B. M. Welsh, "Remote sensing of atmospheric turbulence and transverse atmospheric winds using optical reference sources," *Proc. SPIE*, vol. 1968, no. 1, pp. 229–237, 1993. [Online]. Available: http://dx.doi.org/doi/10.1117/12.154826

[15] T. i Wang, S. F. Clifford, and G. R. Ochs, "Wind and refractive-turbulence sensing using crossed laser beams," *Appl. Opt.*, vol. 13, no. 11, pp. 2602–2608, Nov 1974. [Online]. Available: http://ao.osa.org/abstract.cfm?URI=ao-13-11-2602

[16] S. Oya, M. Takabe, and T. Aruga, "Application of an exclusively binarized correlation-calculation method to wind velocity measurement by use of stellar scintillation patterns," *Appl. Opt.*, vol. 40, no. 24, pp. 4041–4049, Aug 2001. [Online]. Available: http://ao.osa.org/abstract.cfm?URI=ao-40-24-4041

DOI: 01.IJRTET.06.02.195

[17] T. i Wang, G. R. Ochs, and R. S. Lawrence, "Wind measurements by the temporal cross-correlation of the optical scintillations," *Appl. Opt.*, vol. 20, no. 23, pp. 4073–4081, Dec 1981. [Online]. Available:http://ao.osa.org/abstract.cfm?URI=ao-20-23-4073

[18] M. B. Roopashree, A. Vyas, and B. R. Prasad, "Multilayered temporally evolving phase screens based on statistical interpolation," B. L. Ellerbroek, M. Hart, N. Hubin, and P. L. Wizinowich, Eds., vol. 7736, no. 1. *SPIE*, 2010, p. 77363Z. [Online]. Available: http://link.aip.org/link/?PSI/7736/77363Z/1

[19] M. Sch¨ ock and E. J. Spillar, "Measuring wind speeds and turbulence with a wave-front sensor," Opt. Lett., vol. 23, no. 3, pp. 150–152, Feb 1998. [Online]. Available:http://ol.osa.org/abstract.cfm?URI=ol-23-3-150

[20] M. B. Roopashree, V. Akondi, and R. P. Budihala, "Real-time wind speed measurement using wavefront sensor data," *Proc. SPIE*, vol. 7588, no. 1, p. 75880A, 2010. [Online]. Available: http://dx.doi.org/doi/10.1117/12.841333

[21] R. W. Wilson, "Slodar: measuring optical turbulence altitude with a shackhartmann wavefront sensor," *Monthly Notices of the Royal Astronomical Society*, vol. 337, no. 1, pp. 103–108, 2002. [Online].Available:http://dx.doi.org/10.1046/j.1365-8711.2002.05847.x

[22] T. Fusco, G. Rousset, D. Rabaud, E. Gendron, D. Mouillet, F. Lacombe, G. Zins, P.-Y. Madec, A.-M. Lagrange, J. Charton, D. Rouan, N. Hubin, and N. Ageorges, "NAOS on-line characterization of turbulence parameters and adaptive optics performance," *Journal of Optics A: Pure and Applied Optics*, vol. 6, no. 6, p. 585, 2004. [Online]. Available: http://stacks.iop.org/1464-4258/6/i=6/a=014

[23] M. Roopashree, V. Akondi, and R. P. Budihal, "Automated ROI selection and calibration of a microlens array using a MEMS CDM," in Adaptive Optics: Methods, Analysis and Applications. Optical Society of America, 2011, p. ATuA5. [Online]. Available: http://www.opticsinfobase.org/abstract.cfm?URI=AO-2011-ATuA5

[24] M. B. Roopashree, A. Vyas, and B. R. Prasad, "Experimental evaluation of centroiding algorithms at different light intensity and noise levels," AIP Conference Proceedings, vol. 1391, 2011.

[25] W. H. Southwell, "Wave-front estimation from wave-front slope measurements," J. Opt. Soc. Am., vol. 70, no. 8, pp. 998–1006, Aug 1980. [Online]. Available:http://www.opticsinfobase.org/abstract.cfm?URI=josa-70-8-998

[26] K. L. Baker and M. M. Moallem, "Iteratively weighted centroiding for shack- hartmann wave-front sensors," Opt. Express, vol. 15, no. 8, pp. 5147–5159, Apr 2007. Online]. Available: http://www.opticsexpress.org/abstract.cfm?URI=oe-15-8-5147

[27] V. Akondi, M. B. Roopashree, and R. P. Budihala, "Improved iteratively weighted centroiding for accurate spot detection in laser guide star based shack hartmann sensor," vol. 7588, no. 1, p. 758806, 2010. [Online]. Available: http://dx.doi.org/doi/10.1117/12.841331

M. B. Roopashree is currently a Ph.D. candidate at the Indian Institute of Astrophysics, Bangalore, India. She received her MSc and BSc degrees from the University of Mysore, Mysore.

Akondi Vyas received his MSc degree in Physics from the Sri Sathya Sai Institute of Higher Learning. He is currently a Ph.D. student at the Indian Institute of Astrophysics, Bangalore, India.

B. Raghavendra Prasad received his PhD degree in Physics from the Indian Institute of Science. He is currently an Associate Professor at the Indian Institute of Astrophysics, Bangalore, India.

DOI: 01.IJRTET.06.02.195